Localized cell death focuses mechanical forces during 3D patterning in a biofilm

Munehiro Asally[a], Mark Kittisopikul[a,b,c], Pau Rué[d,e], Yingjie Du[f], Zhenxing Hu[f], Tolga Çağatay[b,c], Andra B. Robinson[b,c], Hongbing Lu[f], Jordi Garcia-Ojalvo[d,e], and Gürol M. Süel[a,1]

[a]Section of Molecular Biology, Division of Biological Sciences, University of California at San Diego, La Jolla, CA 92093; [b]Department of Pharmacology and [c]Green Center for Systems Biology, University of Texas Southwestern Medical Center, Dallas, TX 75390; [d]Departament de Física i Enginyeria Nuclear, Universitat Politècnica de Catalunya, E-08222 Terrassa, Spain; [e]Department of Experimental and Health Sciences, Universitat Pompeu Fabra, 08003 Barcelona, Spain; and [f]Department of Mechanical Engineering, University of Texas at Dallas, Richardson, TX 75080

Edited* by Herbert Levine, University of California at San Diego, La Jolla, CA, and approved August 27, 2012 (received for review July 19, 2012)

From microbial biofilm communities to multicellular organisms, 3D macroscopic structures develop through poorly understood interplay between cellular processes and mechanical forces. Investigating wrinkled biofilms of *Bacillus subtilis*, we discovered a pattern of localized cell death that spatially focuses mechanical forces, and thereby initiates wrinkle formation. Deletion of genes implicated in biofilm development, together with mathematical modeling, revealed that ECM production underlies the localization of cell death. Simultaneously with cell death, we quantitatively measured mechanical stiffness and movement in WT and mutant biofilms. Results suggest that localized cell death provides an outlet for lateral compressive forces, thereby promoting vertical mechanical buckling, which subsequently leads to wrinkle formation. Guided by these findings, we were able to generate artificial wrinkle patterns within biofilms. Formation of 3D structures facilitated by cell death may underlie self-organization in other developmental systems, and could enable engineering of macroscopic structures from cell populations.

pattern formation | self-assembly | systems dynamics

Self-organization in space and time is a fundamental developmental process, defined by the autonomous formation of 3D macroscopic structures by replicating cell populations (1–3). Such 3D pattern formation underlies the development of all multicellular organisms and cellular communities, and appears to be governed by two principal processes. First, genetic programs control cellular processes, such as growth, death, and differentiation. Second, 3D structure formation involves macroscopic movement of cell populations that are determined by mechanical properties and physical forces (4). Recent studies have investigated each of these processes separately in different biological systems (5–8). However, insight into the direct interplay between cellular and mechanical processes that drives development requires simultaneous measurement of both processes, and thus constitutes a major challenge.

Compared with multicellular organisms, microbial biofilms are simpler systems for investigating the interaction between cellular and mechanical aspects of 3D self-organization during development. Interestingly, these microbial communities still exhibit diverse cellular behaviors and complex spatial organization (9–14). For example, biofilms can develop from a single cell and give rise to complex 3D wrinkle structures that are visible to the naked eye, comprising billions of cells (9, 10, 15) (Fig. 1*A*). Aside from replication, bacterial cells can also exhibit other behaviors, such as genetically controlled cell death (9, 16, 17) and excretion of ECM components (9, 13, 18–21). In fact, one of the defining features of any biofilm is that cells are embedded within an ECM composed of diverse molecules, such as polysaccharides and amyloid fibers (19–21). The ECM is required for wrinkle formation and appears to provide the biofilm with resilience against environmental extremes as well as mechanical support (9, 20–22). It is also conceivable that replicating cells within the ECM can generate forces by pushing against each other, whereas cell death could provide an outlet for such forces. However, the interplay between mechanical forces and cellular processes, such as cell growth and death, and their role during biofilm development remains unclear.

Here, we investigated the spatiotemporal dynamics of cell death and mechanical processes during self-organization of *Bacillus subtilis* cells into wrinkled biofilms. Specifically, we combined quantitative measurements of cell death, movement, and mechanical properties to analyze development of WT and mutant biofilms. These measurements were obtained with fluorescence time-lapse microscopy, tracking of fluorescent beads embedded within biofilms, and atomic force microscopy (AFM) nanoindentation, respectively. Our findings suggest that lateral mechanical forces build up during biofilm growth and expansion, and are then focused in space by localized cell death, thus triggering vertical buckling and subsequent wrinkle formation. The formation of wrinkle structures facilitated by cell death may constitute a population-level stress response of biofilms. These insights could allow the engineering of desired macroscopic structures from cellular populations in the future and provide exciting opportunities at the interface between synthetic biology and material sciences.

Results

Cell Death and Wrinkle Structures Correlate in Space. Multicolor fluorescence and transmission EM imaging of biofilms indicated that cell death and wrinkles are spatially correlated. We imaged cross-sections of *B. subtilis* biofilms that contained fluorescent reporters for dividing cells and death (Fig. 1 *B* and *C*). In particular, we used expression of CFP from the promoter of the cell division operon *ftsAZ* as a reporter for cell density (23) (Fig. 1*C*, gray). At the same time, we measured cell death using Sytox Green, a commercially available fluorescent marker of cell death (Fig. 1*C*, green). This high-affinity nucleic acid stain only penetrates permeabilized cells and has been established as a specific reporter for cell death in various systems, including *B. subtilis* (24, 25) (Fig. S1 *A* and *B*). Importantly, this reporter does not affect biofilm formation (Fig. S1*C*). Cross-sections of biofilms revealed that cell death is localized at the bottom of biofilms, and more specifically at the center of folded wrinkle structures (Fig. 1*C*). Transmission EM confirmed the presence of dead cells at the bottom of wrinkle interfaces (Fig. 1*D*). These findings are

Author contributions: M.A., M.K., P.R., J.G.-O., and G.M.S. designed research; M.A., P.R., Y.D., Z.H., and A.B.R. performed research; M.A., M.K., P.R., T.Ç., and J.G.-O. contributed new reagents/analytic tools; M.A., M.K., Y.D., Z.H., H.L., and G.M.S. analyzed data; and M.A., J.G.-O., and G.M.S. wrote the paper.

The authors declare no conflict of interest.

*This Direct Submission article had a prearranged editor.

Freely available online through the PNAS open access option.

[1]To whom correspondence should be addressed. E-mail: gsuel@ucsd.edu.

This article contains supporting information online at www.pnas.org/lookup/suppl/doi:10.1073/pnas.1212429109/-/DCSupplemental.

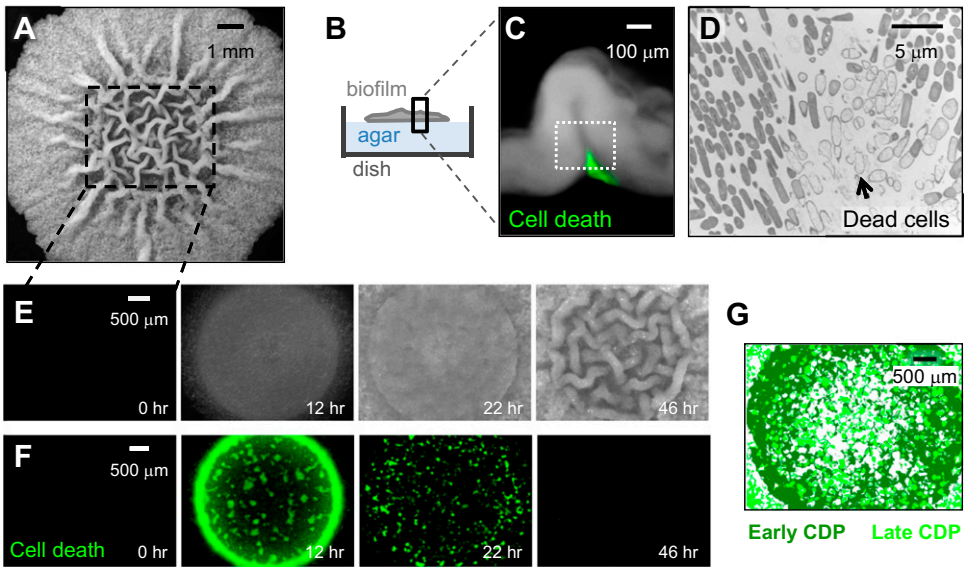

Fig. 1. Localized pattern of cell death correlates with the site of wrinkles in biofilms. (*A*) Three-day-old *B. subtilis* biofilm structure. The dashed square indicates the region of interest in this study. (*B*) Schematic of the microscope setting for fluorescent and bright-field imaging of a biofilm (depicted in gray). Dashed lines indicate the direction of observation. (*C*) Cross-section florescence image of a 30-h-old biofilm wrinkle, pseudocolored (P*ftsAZ*-CFP in gray and a cell death reporter Sytox in green). (*D*) Transmission electron (TEM) micrograph of a sectioned biofilm wrinkle shows dead cells (black arrow) in the wrinkle interior (white box in *C* depicts observed location). (*E*) Film strip shows biofilm morphology observed from above the colony. (*F*) Film strip shows CDP during early (~22 h) development of biofilm, imaged from below. Brightness and contrast are individually adjusted for each time point. (*G*) Early (dark green) and late (light green) CDPs detected by a correlation-based clustering analysis (*SI Materials and Methods*) of Sytox time-lapse images.

consistent with at least two scenarios, namely, that wrinkle formation results in the death of cells or that cell death occurs first and perhaps facilitates wrinkle formation.

To discriminate between these possible scenarios, we began by measuring the spatiotemporal dynamics of cell death during *B. subtilis* biofilm development using fluorescence time-lapse microscopy. Unexpectedly, measurements uncovered a striking heterogeneous distribution of cell death that occurs before wrinkle formation (Fig. 1 *E*–*G*). A similarly heterogeneous cell death pattern (CDP) is generated even when the biofilm is started from a single cell (Fig. S1*E*). Together, these data suggest that the replicating cell population during biofilm development gives rise to a heterogeneous CDP that may be genetically controlled.

Gene Deletion Analysis Reveals Genetic Control of the CDP. To identify genetic control of the CDP, we deleted 32 genes involved in eight diverse aspects of biofilm development and analyzed the resulting CDPs quantitatively (Fig. 2 *A*–*F*). Specifically, we analyzed at least three movies for each mutant strain and generated overlaid images representing a simplified history of when and where cell death occurred (Fig. 1*G*, Fig. S2, and *SI Materials and Methods*). We then quantified the spatial complexity (heterogeneity) of this CDP. In particular, we calculated the perimeter-to-area ratio ($P^2/4\pi A$, where P is the perimeter and A is the area) for all CDPs so as to assign a numerical value to their complexity (Fig. 2*A* and *SI Materials and Methods*). This ratio is equal to unity for a perfect circular pattern and has a higher value for more complex patterns (WT CDP = 2,337 ± 623, n = 12). This analysis allowed us to identify the connection between gene activities and the spatiotemporal heterogeneity of the CDP (Fig. 2*A*).

The most pronounced change in the CDP phenotype is generated by deletion of genes implicated in ECM production. These genes appear to be required to generate localized cell death. Specifically, five gene deletion strains generated CDPs with statistically significant ($P < 0.01$) decreased spatial heterogeneity. Three of those genes, *srfA*, *spo0A*, and *sinI*, are known to regulate, among others, matrix production through cell-to-cell signaling and transcriptional regulation. The other two genes, *tasA* and *epsH*, are directly involved in production of the ECM. In particular, the *tasA* gene expresses an extracellular protein that forms amyloid fibers within the matrix (19), whereas the *epsH* gene is necessary for synthesis of polysaccharides that comprise the biofilm ECM (10). Deletion of the *epsH* gene resulted in a CDP with the lowest spatial heterogeneity, where cell death occurred globally and homogeneously (Fig. 2*F*). Consistent with our findings (Fig. 2 *A*–*F*), colony wrinkle morphology has been shown to diminish with matrix deficiency (10, 13, 14, 19). Here, we further show that these mutant biofilms also exhibit reduced CDP heterogeneity before deficiency in wrinkle morphologies becomes evident. These results demonstrate that expression of matrix components contributes to the heterogeneity of the CDP in both space and time.

We also identified gene deletions that reduced cell death without changing the spatial pattern. Specifically, deletion of two environmental stress-dependent toxin genes (*spoIISAB* and *ndoAI*) reduced cell death by 25 ± 7% (Fig. 2*C* and Fig. S3), suggesting that death occurs due to build-up of local biochemical stress (26–29). The notion of local biochemical stress-induced death is furthermore supported by the following results: (*i*) Cell death is first observed at regions of initial high cell density (Fig. S1*D*), and (*ii*) cell death is heterogeneous and highly localized in space (Fig. 1*F*). Together, these data imply that biochemical stress builds up locally during biofilm development, and thereby gives rise to the observed CDP. Furthermore, this mutant strain with reduced cell death also generated biofilms with visibly diminished wrinkle morphology (Fig. 2*C*). Reduction of cell death thus appeared to have an unfavorable consequence on wrinkle formation, even though the spatial pattern of death was unchanged from WT (Fig. 2*A*). Altogether, the gene deletion results imply that localized cell death may contribute to wrinkle formation during biofilm development.

Population-Level Mathematical Model Accounts for the CDP. We asked if a mesoscopic mathematical model of population growth, based on our findings described above, could account for the

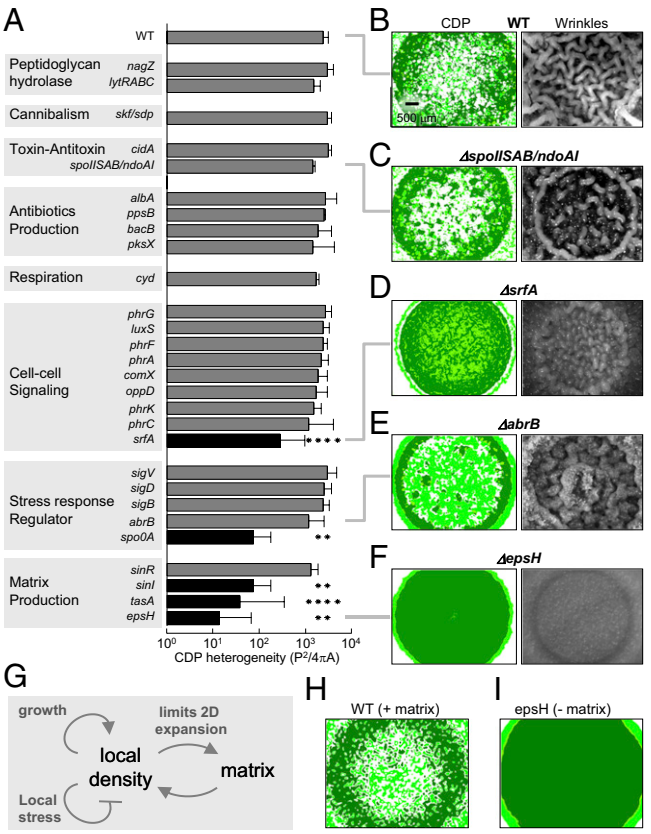

Fig. 2. Gene deletion analysis reveals that ECM production is required for the CDP. (*A*) KO strains are categorized and listed by their functions. The CDP heterogeneity (perimeter squared over the area) of the late CDP (light green) is graphed for each deletion strain (mean ± SD). Asterisks and black shading indicate *P* values (***P* < 0.01; *****P* < 0.0001) evaluated using Tukey's Honestly Significant Difference test. Representative clustered CDP images as in Fig. 1*G* (*Left*) and colony morphology (*Right*) of WT (*B*), *ΔspoIISAB/ndoAI* (*C*), *ΔsrfA* (*D*), *ΔabrB* (*E*), and *ΔepsH* (*F*) strains. The scale for *B*–*F* is as indicated in *B*. (*G*) Schematic of the mathematical model in which local cell density is governed by density-dependent growth and death and the ECM maintains density by preventing expansion (details are provided in *SI Text*). The CDPs are generated by the mathematical model. Simulations with (*H*) and without (*I*) matrix production are processed using the same correlation-based clustering analysis as experimental data.

complex CDP. Similar to previous theoretical approaches to microbial pattern formation (30), our model is based on a system of coupled partial differential equations that determine local cell density as a function of space and time (Fig. 2*G* and *SI Text*). This phenomenological model makes the following four simple assumptions that were based on and constrained by experimental observations (the parameters are listed in Table S1): (*i*) Local cell density is increased by heterogeneous growth, based on experimental measurements of the spatial distribution of metabolically active cells (Fig. S4*C*); (*ii*) cell death occurs when density exceeds the carrying capacity, due to build-up of local biochemical stress, as supported by the experimental observations detailed above; (*iii*) increase in local cell density by cell replication is counteracted by the tendency of high density to spread out in space; and (*iv*) expression of ECM counteracts the expansion of local cell density, consistent with comparative measurements in WT and *epsH* deletion strains (see Fig. S7*A*).

The model accounts for the basic spatiotemporal dynamics of the WT CDP (Fig. 2*H*), and it does so robustly with respect to parameter variation (Fig. S5 and *SI Text*). Additionally, when matrix production is turned off in the model, the simulations generate a homogeneous CDP similar to that observed in the *epsH* deletion strain (Fig. 2*I*). Simulations approximating dilute starting culture conditions are also consistent with experimental observations (Fig. S4 *G* and *H* and *SI Text*). Therefore, this population-level model accounts for the observed heterogeneity of the CDP, and thereby provides a conceptual explanation for how the ECM can promote a localized pattern.

Quantitative Tracking of Movement During Wrinkle Formation. In addition to its role in localized cell death presented here, the matrix is required to generate wrinkled biofilms (10, 19, 22). To determine quantitatively where and when wrinkle formation occurs, we measured movement within the biofilm. Specifically, we tracked movement of fluorescent beads mixed in with the starting culture to measure wrinkle formation dynamics quantitatively (Fig. 3*A*). We determined the trajectories of beads that were displaced by movement within the developing biofilm (Fig. 3*B*). From these trajectories, we calculated the corresponding velocity vector field of movement (*SI Materials and Methods*). The resulting data identified local areas at which the velocity field exhibits convergence (or negative divergence) (Fig. 3*C*), which corresponds to velocity vectors pointing toward each other (Fig. 3*B*). Furthermore, we observe disappearance of beads from the focal plane at convergence centers (Movie S1). Together with the convergence of lateral movement, these results suggest that the biofilm is pushed in the *z* dimension, and thus may be undergoing vertical buckling (Fig. 3*D*).

We investigated if vertical buckling could lead to the formation of wrinkles. To test this prediction, we calculated what the 3D wrinkle pattern would look like based on the measured convergence pattern (Fig. 3*E*). Specifically, we used the magnitude of convergence to assign wrinkle height in the *z* dimension. We then compared the simulated results with experimentally determined 3D topographies of wrinkle patterns in biofilms that were obtained using stereomicroscopy (Fig. 3*F*). As predicted, we find that the convergence pattern overlaps in space with the experimentally observed wrinkle (Fig. 3*G*). These findings support the idea that wrinkles form through vertical buckling within the biofilm.

Mechanical Stiffness of Biofilms Influences Wrinkle Formation Rate and Pattern. Generation of wrinkles by buckling suggests that wrinkle formation would depend on the mechanical properties of the biofilm, which are, at least in part, governed by the ECM. This hypothesis is consistent with studies that have shown ECM production to be necessary for wrinkled biofilm formation (10, 19, 22). To investigate the possible role of mechanical forces in wrinkle formation, we turned to material sciences studies of wrinkling in the bonded, thin-layered films that are commonly used in optical coatings and electronic devices, such as microprocessors. We used these studies because, as the name implies, biofilms constitute thin biological films composed of bacterial cells that are embedded within an ECM. Material sciences studies have shown that the stiffness (Young's modulus) of such thin films determines the width of the wrinkle pattern (i.e., how far wrinkles are apart) as well as its formation rate (31, 32).

To test whether this prediction also applies to biofilms, we used AFM nanoindentation measurements to determine mechanical stiffness accurately. We used *ΔabrB* and *ΔsrfA* strains suggested to generate biofilms with varying stiffness (stiffer or softer relative to WT) due to differences in ECM production. In particular, the *abrB* gene product is a well-characterized repressor of ECM production (33); therefore, its deletion is expected to generate a stiffer biofilm. In contrast, activity of the *srf* operon promotes ECM production (34); thus, its deletion is expected to generate a softer biofilm. Unfortunately, biofilms formed by the *epsH* mutant were too soft (<3 kPa) to measure with our experimental AFM setup, but we obtained reproducible

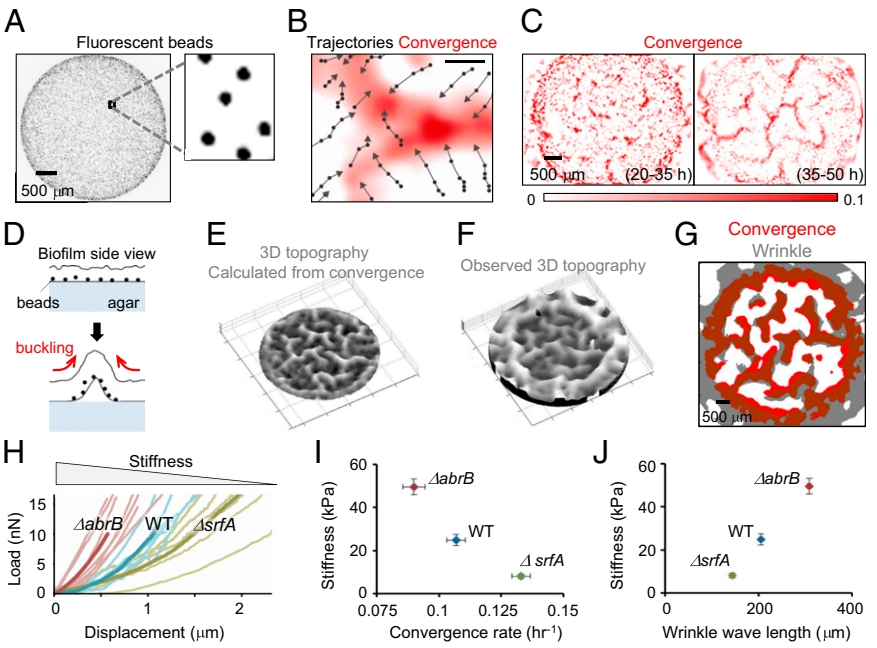

Fig. 3. Movement reveals that wrinkle formation in the biofilm is generated by mechanical buckling. (*A*) Fluorescent beads (black) mixed with cells from the beginning of biofilm formation are shown in an inverted fluorescence image. (*B*) Movements of beads during biofilm formation are tracked, and their trajectories are shown as black arrows and dots. (Scale bar: 50 μm.) (*B* and *C*) Convergence (negative divergence) field (red) of the interpolated vector field calculated from bead trajectories. Convergence images obtained from movements in the time window are indicated in *C*. (*D*) Schematic of the hypothesis shows convergence resulting in buckling and wrinkle formation. (*E*) Three-dimensional surface plot predicted from a convergence field after spatial averaging. (*F*) Three-dimensional surface plot of the same biofilm as in *E* observed from above using stereomicroscopy in the same orientation as in *E*. (*G*) Areas from *E* (red) and *F* (gray) above the respective thresholds represent wrinkle locations merged in two dimensions. (*H*) Load-displacement curves of WT, Δ*srfA*, and Δ*abrB* obtained by AFM nanoindentation. The faded lines indicate actual measurements results, and the thick lines represent their mean curves. The stiffness (Young's modulus: tensile stress divided by tensile strain) of each biofilm strain is calculated using these load-displacement curves. The maximum convergence rate determined from each convergence time trace (Fig. S6*C*) (*I*) and the wrinkle width (*J*) are plotted against stiffness (Young's modulus) for WT, Δ*srfA*, and Δ*abrB* (mean ± SEM).

measurements for the *abrB* and *srfA* mutant strains. We quantified the mechanical stiffness (Young's modulus) of these biofilms using AFM nanoindentation (Fig. 3*H*). As expected, the *abrB* deletion strain generated the most rigid biofilm (49.6 ± 3.7 kPa, $n = 16$) followed by WT (25.0 ± 2.5 kPa, $n = 19$) and the *srfA* deletion strain (8.1 ± 1.1 kPa, $n = 17$) (Fig. 3*H* and Fig. S6 *A* and *B*). For all three strains, we then quantified convergence of bead movements during biofilm formation (as described above) to determine the rate of wrinkle formation. Consistent with theoretical predictions developed for layered thin films, we find a negative correlation between mechanical stiffness and the rate of wrinkle formation in biofilms (Fig. 3*I*). Furthermore, we find a positive correlation between stiffness and the width of the wrinkle pattern (Figs. 2 *B*, *D*, and *E* and 3*J*), which is also consistent with predictions (31, 32). Together, these results demonstrate that the mechanical stiffness of the biofilm, at least in part determined by the ECM, is a key property that determines wrinkle formation pattern and dynamics during biofilm development.

Localized Cell Death Focuses Mechanical Forces in Space and Thereby Facilitates Wrinkle Formation. Next, we simultaneously measured bead trajectories and the CDP, which revealed that convergence of movement and localized cell death overlap in space but are separated in time. Specifically, localized cell death (18 h) occurs first and is then followed by convergence (20–35 h). Magnified images clearly show that convergence within the velocity field is directed toward the center of the preceding region of cell death (Fig. 4 *A*–*C*). As expected, convergence was not observed in the *epsH* deletion strain, which undergoes global and homogeneous cell death (Fig. S7*A*). Therefore, localized cell death not only precedes convergence of movement (Fig. 4*D*) but, more specifically, appears to focus the velocity field in space. Further analysis confirms that the CDP is predictive of the convergence pattern that emerges with a time delay of ~6 ± 0.8 h (based on cross-correlation analysis, $n = 6$) (Fig. 4*E*). We note that facilitation of wrinkle formation by localized cell death is more pronounced in stiffer biofilms, which would either require larger forces or longer time scales to undergo buckling (Fig. 4*F*). These data suggest that regions of cell death provide a localized outlet for mechanical forces. Therefore, wrinkle formation appears to be initiated by localized cell death, which spatially focuses lateral forces, and thereby promotes vertical buckling of the biofilm (Fig. 4*G*).

To test our finding that cell death facilitates wrinkle formation, we introduced an artificial pattern of cell density and death to generate synthetic wrinkle patterns (Fig. 4*H*). Specifically, we manually applied cells to the agar plate over the typical starting culture to generate local regions of higher cell density. As expected, these regions of high cell density gave rise to local cell death, which, in turn, generated a matching wrinkle pattern (Fig. 4*H*). Using this approach, we were able to generate large wrinkles within the biofilm reliably at arbitrary sites of our choosing (Fig. S7 *C* and *D*). In addition, direct induction of buckling by local mechanical perturbation of the biofilm generated artificial wrinkles (Fig. S7 *E* and *F*). These results further suggest that localized cell death provides an outlet for build-up compressive forces and focuses them in space, thereby resulting in buckling and consequent wrinkle formation. Self-assembly of the bacterial biofilm can thus be controlled through these principles to engineer synthetic wrinkle structures.

Discussion

In this study, we show that death is nonuniform in space and time during biofilm formation, and appears to give rise to mechanical forces that can generate macroscopic 3D structures. Specifically, our quantitative description of the direct interaction between cellular and mechanical processes reveals that localized cell death and wrinkle formation comprise an ordered and controlled process during biofilm development. Any microbial biofilm that exhibits cell growth and death in combination with production of an ECM would be subject to mechanical forces like those characterized here. Furthermore, we note that the nucleation of wrinkle formation by cell death suggests that partial killing of bacterial cells in biofilms can enhance wrinkle formation. This notion could explain why increased wrinkle formation is observed in biofilms that experience greater cell death as a result of treatment with an antimicrobial agent (35). It is possible that partial killing of bacteria in biofilms enhances their resilience against environmental extremes through increased wrinkle formation, because wrinkling contrib-

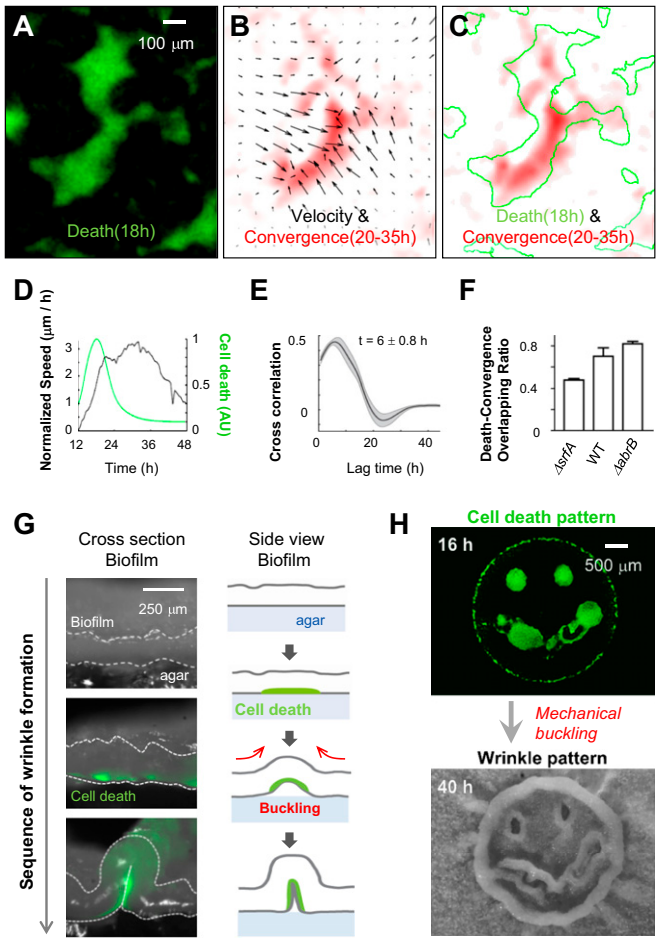

Fig. 4. Localized cell death facilitated mechanics of wrinkle formation. Magnified view of localized cell death at 18 h (*A*), velocity field (arrows) and convergence (red) of the same location (*B*), and merged image of convergence (red, 20–35 h) and cell death outline (green, 18 h) (*C*). The scale for *A*–*C* is as indicated in *A*. (*D*) Average speed of fluorescent beads in the *ΔepsH* strain subtracted from that of the WT strain (black line: $Speed_{wt} - Speed_{\Delta epsH}$) ($n = 3$). The Sytox intensity (green) is shown for WT. The individual time traces for WT and *ΔepsH* are provided in Fig. S4*A*. AU, arbitrary unit. (*E*) Cross-correlation curve (between cell death and convergence) of localized cell death regions analyzed with individual biofilms. The calculated time delay ($\tau = 6 \pm 0.8$ h, mean ± SEM, $n = 5$) is the temporal offset that gives the maximum cross-correlation value between cell death and convergence. (*F*) Ratio of high-convergence regions that spatially correlate with local early cell death, measured for the WT, *ΔsrfA*, and *ΔabrB* strains (mean ± SEM, $n = 3$). (*G*) Cross-sectional images and schematic of the wrinkle formation process (green: cell death, light blue: agar medium). (*H*) Artificial smiley face CDP (*Upper*) created by painting higher cell density areas and a matching wrinkle pattern (*Lower*).

utes to higher resistance against liquid wetting and gas penetration (15). Therefore, we suggest that localized cell death constitutes a community-level stress response to enhance biofilm resistance under unfavorable conditions.

Mechanical forces arising from cell death reported here for biofilm development can potentially provide a conceptual framework for observations made in other biological systems, including multicellular organisms. For example, recent work has suggested that apoptosis facilitates dorsal closure during *Drosophila* embryogenesis (36). Similar to the buckling of the biofilm triggered by local cell death, dorsal closure in *Drosophila* appears to be aided by the buckling of surrounding tissue toward the site of apoptosis. Even though the mechanism of cell death may differ, in both cases, localized cell death appears to focus mechanical forces in space to drive macroscopic movement. Therefore, utilization of localized cell death as a means to focus and direct mechanical forces spatially may be a general mechanism underlying the generation and alteration of macroscopic 3D structures during development. Furthermore, it may be possible to test and enhance our understanding of development in natural systems by attempting to design and engineer synthetic 3D patterns rationally from living organisms (3, 11, 12). Synthetic self-organization through control over localized cell death could also serve as a tool to generate mechanical forces and perturb biological systems to investigate the interplay between cellular and mechanical processes directly in biology.

Materials and Methods

Strains and Growth Conditions. Table S2 lists the *B. subtilis* strains used in this study. All strains were routinely grown in LB or LB agar plates at 37 °C. When appropriate, antibiotics were supplemented in LB at the following concentrations: 100 μg/mL ampicillin, 8 μg/mL neomycin, 300 μg/mL spectinomycin, and 5 μg/mL chloramphenicol. All strains were derived from the undomesticated WT *B. subtilis* strain NCIB3610.

Strain Constructions. Strains were created by a standard method using chromosomal integration vectors after sequence confirmation. All transformations of the NCIB3610 strain were performed by a standard one-step transformation procedure (37). For the deletion constructs, plus-strand regions of target genes were amplified from NCIB3610 by PCR using specific primers. Amplified fragments were cloned into *B. subtilis* chromosomal integration vector pER449 (a kind gift from the laboratory of Wade Winkler, University of Maryland, College Park, MD). The resulting target deletion constructs were confirmed by direct sequencing and integrated into the chromosome of NCIB3610 by homologous recombination. The plasmid pSac-Cm (ECE174; Bacillus Genetic Stock Center) was used for integration to the *sacA* locus. Chromosomal integrations were confirmed by colony PCR using specific primers.

Biofilm Formation. *B. subtilis* strains were picked from overnight growth on LB plates and cultured in LB at 37 °C. Saturated culture was grown in MSgg [5 mM potassium phosphate (pH 7.0), 100 mM 3-(*N*-morpholino)propanesulfonic acid (pH 7.0), 2 mM $MgCl_2$, 700 μM $CaCl_2$, 50 μM $MnCl_2$, 100 μM $FeCl_3$, 1 μM $ZnCl_2$, 2 μM thiamine, 0.5% glycerol, 0.5% glutamate] for 1 h and was then spotted on an MSgg plate (MSgg medium supplemented with 1.5% agar, 3 mm thickness, dried overnight) and incubated at 30 °C (10). For the fluorescent bead tracking, cell culture was mixed with beads (3.6×10^3 per colony) (FluoSpheres Carboxylate-Modified Microspheres, 1.0 μm, Yellow-Green Fluorescent; Invitrogen) before plating on MSgg. Mixing the beads was confirmed not to affect the biofilm formation. When appropriate, Sytox dead cell stain (Invitrogen) was supplemented into MSgg medium, with a final concentration of 0.5 μM and 1 μM for Sytox Green and Blue (Invitrogen), respectively. For cross-section images of biofilm, colonies were manually sliced by razor and imaged by a Retiga 2000R digital camera (QImaging) via an SZX10 fluorescent stereomicroscope (Olympus).

A heterogeneous cell density pattern was generated using two steps to apply cells. First, cells were spotted onto an MSgg agar plate and dried for 30 min at 37 °C. On top of this low-density layer, a cell suspension concentrated 10-fold from overnight culture was locally applied using a fine paint brush. As a negative control, double-distilled water (dDW) was used instead of the concentrated cells. Wrinkles were observed after 2 d of incubation at 30 °C.

EM Image. An overnight culture of WT *B. subtilis* was spotted onto MSgg agar plates and incubated at 30 °C for 20 h. Bacterial colonies were fixed with 2.5% glutaraldehyde in 0.1 M sodium cacodylate buffer, postfixed in 1% buffered osmium tetroxide, en bloc-stained in 4% uranyl acetate, dehydrated with a graded series of ethanol, and embedded in EMbed-812 resin (EMbed). Thin sections (80 nm) were cut on an EM UC6 ultramicrotome (Leica) and stained with 2% uranyl acetate and lead citrate. Images were acquired on a Tecnai G2 Spirit transmission electron microscope (FEI) equipped with a LaB6 source and operating at 120 kV.

Time-Lapse Microscopy. Time-lapse movies were obtained with custom software for automated image acquisition and microscope control. *B. subtilis* strains were applied onto a 1.5% agar pad made with MSgg medium supplemented with Sytox Green or Blue. Time series of images were acquired by an ORCA-ER digital camera (Hamamatsu) via an IX71 fluorescence microscope (Olympus) every 40 min at 30 °C. Cells were diluted 50-fold in dDW before application onto the pad for the single-cell movies. Biofilm movies

were made from the bottom using an objective lens (MPLFLN 2.5×/0.08; Olympus) with a long working distance. Collected images were processed with ImageJ (National Institutes of Health, http://imagej.nih.gov/ij/) (38) and MATLAB (MathWorks).

Three-Dimensional Surface Topology Measurement. To measure the height of the *B. subtilis* biofilm (4-d-old) structures, we used an OPM-1 stereomicroscope (Zeiss) that is based on a binocular vision system, also known as 3D digital image correlation (39). After determining the relative positions of the two cameras and intrinsic parameters, the shape of the specimen was reconstructed from the point correspondences using triangulation. Classic camera calibration approaches typically start from the ideal pinhole camera model, to which the parametric of the distortion functions are added to account for the distortion of each optical element. A 0.2-mm square-dimension chessboard (Texas Industrial Optics, Inc.) was used as the calibration board. To generate the mapping function, a flat glass slide with random paint speckles was imaged at fixed translations during in-plane motions on a 6-df stage (Optics Edmunds). Biofilm images were taken with the light source behind the biofilm to avoid the decorrelation effect of light coming from the observing side.

Stiffness Measurement. From nanoindentation measurements, Young's modulus of the biofilm was calculated by fitting the load-displacement curve with the Hertz model (40). The Hertz model for indentation depth by a conical indenter is $F = \frac{2E_r\delta^2}{\pi(1-\nu)}\tan\alpha$, where F is the loading force, ν is Poisson's ratio (assusmed to be 0.3), δ is the indentation depth, α is the half-angle of a conical indenter, and E_r is the reduced modulus. Young's modulus of the sample can be obtained by $\frac{1}{E_r} = \frac{1-\nu_i^2}{E_i} + \frac{1-\nu_s}{E_s}$, where E_i and E_s are the moduli of the indenter tip and sample, respectively, and ν_i and ν_s are Poisson's ratio of the indenter tip and sample, respectively. Nanoindentation measurements were conducted on an MFP-3D stand-alone AFM machine (Asylum). A conical tip with a half-angle of 30° and a spring constant of 0.32 N/m was used for nanoindentation. All measurements were conducted in 100% glycerol at room temperature. The indentations were performed in the center area of 7-d-old biofilms. Two rounds of measurements were performed to verify the consistency of these tests. Igor Pro-6.22 (Igor) and its Asylum subroutine installed on the AFM machine were used to do nanoindentation elastic analysis. Statistical analysis was performed using GraphPad Prism.

Image Analysis. The image analysis is detailed in *SI Materials and Methods*.

ACKNOWLEDGMENTS. We thank Drs. M. Heinemann, M. Lehrman, S. Lockless, M. Rosen, R. Ranganathan, K. Süel, and D. Sprinzak and members of the G.M.S. laboratory for comments on the manuscript; Drs. W. Winkler, R. Kolter, and K. Pogliano for kindly providing bacterial strains; and H. Wu for analyzing time-lapse images. H.L. acknowledges funding from National Science Foundation Grants DMR-0907291, CMMI-1031829, and 1132174 and National Institutes of Health Grants 1 R01 EB013212 and 1 R01 DC011585. J.G.O. acknowledges funding from Grant FIS2009-13360 from the Spanish Ministry of Economy and Competitiveness and the Institució Catalana de Recerca i Estudis Avançats Academia Programme. This research was funded by National Institutes of Health National Institute of General Medical Sciences Grant R01 GM088428 and James S. McDonnell Foundation Grant 220020141 (both to G.M.S.).

1. Whitesides GM, Grzybowski B (2002) Self-assembly at all scales. *Science* 295: 2418–2421.
2. Camazine S, et al. (2003) *Self-Organization in Biological Systems* (Princeton Univ Press, Princeton).
3. Woodford C, Zandstra PW (2012) Tissue engineering 2.0: Guiding self-organization during pluripotent stem cell differentiation. *Curr Opin Biotechnol*, in press.
4. Mammoto T, Ingber DE (2010) Mechanical control of tissue and organ development. *Development* 137:1407–1420.
5. Savin T, et al. (2011) On the growth and form of the gut. *Nature* 476:57–62.
6. Uyttewaal M, et al. (2012) Mechanical stress acts via katanin to amplify differences in growth rate between adjacent cells in Arabidopsis. *Cell* 149:439–451.
7. Kierzkowski D, et al. (2012) Elastic domains regulate growth and organogenesis in the plant shoot apical meristem. *Science* 335:1096–1099.
8. Wang Y-C, Khan Z, Kaschube M, Wieschaus EF (2012) Differential positioning of adherens junctions is associated with initiation of epithelial folding. *Nature* 484: 390–393.
9. Webb JS, Givskov M, Kjelleberg S (2003) Bacterial biofilms: Prokaryotic adventures in multicellularity. *Curr Opin Microbiol* 6:578–585.
10. Branda SS, González-Pastor JE, Ben-Yehuda S, Losick R, Kolter R (2001) Fruiting body formation by Bacillus subtilis. *Proc Natl Acad Sci USA* 98:11621–11626.
11. Wood TK, Hong SH, Ma Q (2011) Engineering biofilm formation and dispersal. *Trends Biotechnol* 29:87–94.
12. Markx GH, Andrews JS, Mason VP (2004) Towards microbial tissue engineering? *Trends Biotechnol* 22:417–422.
13. López D, Kolter R (2010) Extracellular signals that define distinct and coexisting cell fates in Bacillus subtilis. *FEMS Microbiol Rev* 34(2):134–149.
14. Vlamakis H, Aguilar C, Losick R, Kolter R (2008) Control of cell fate by the formation of an architecturally complex bacterial community. *Genes Dev* 22:945–953.
15. Epstein AK, Pokroy B, Seminara A, Aizenberg J (2011) Bacterial biofilm shows persistent resistance to liquid wetting and gas penetration. *Proc Natl Acad Sci USA* 108: 995–1000.
16. Bayles KW (2007) The biological role of death and lysis in biofilm development. *Nat Rev Microbiol* 5:721–726.
17. Webb JS, et al. (2003) Cell death in Pseudomonas aeruginosa biofilm development. *J Bacteriol* 185:4585–4592.
18. Seminara A, et al. (2012) Osmotic spreading of Bacillus subtilis biofilms driven by an extracellular matrix. *Proc Natl Acad Sci USA* 109:1116–1121.
19. Romero D, Aguilar C, Losick R, Kolter R (2010) Amyloid fibers provide structural integrity to Bacillus subtilis biofilms. *Proc Natl Acad Sci USA* 107:2230–2234.
20. Marvasi M, Visscher PT, Casillas Martinez L (2010) Exopolymeric substances (EPS) from Bacillus subtilis: Polymers and genes encoding their synthesis. *FEMS Microbiol Lett* 313(1):1–9.
21. Flemming H-C, Wingender J (2010) The biofilm matrix. *Nat Rev Microbiol* 8:623–633.
22. Kearns DB, Chu F, Branda SS, Kolter R, Losick R (2005) A master regulator for biofilm formation by Bacillus subtilis. *Mol Microbiol* 55:739–749.
23. Gonzy-Tréboul G, Karmazyn-Campelli C, Stragier P (1992) Developmental regulation of transcription of the Bacillus subtilis ftsAZ operon. *J Mol Biol* 224:967–979.
24. Roth BL, Poot M, Yue ST, Millard PJ (1997) Bacterial viability and antibiotic susceptibility testing with SYTOX green nucleic acid stain. *Appl Environ Microbiol* 63: 2421–2431.
25. Lamsa A, Liu W-T, Dorrestein PC, Pogliano K (2012) The Bacillus subtilis cannibalism toxin SDP collapses the proton motive force and induces autolysis. *Mol Microbiol* 84: 486–500.
26. Wang X, Wood TK (2011) Toxin-antitoxin systems influence biofilm and persister cell formation and the general stress response. *Appl Environ Microbiol* 77:5577–5583.
27. Rešetárová S, Florek P, Muchová K, Wilkinson AJ, Barák I (2010) Expression and localization of SpoIISA toxin during the life cycle of Bacillus subtilis. *Res Microbiol* 161: 750–756.
28. Pellegrini O, Mathy N, Gogos A, Shapiro L, Condon C (2005) The Bacillus subtilis ydcDE operon encodes an endoribonuclease of the MazF/PemK family and its inhibitor. *Mol Microbiol* 56:1139–1148.
29. Wu X, Wang X, Drlica K, Zhao X (2011) A toxin-antitoxin module in Bacillus subtilis can both mitigate and amplify effects of lethal stress. *PLoS ONE* 6:e23909.
30. Fu X, et al. (2012) Stripe formation in bacterial systems with density-suppressed motility. *Phys Rev Lett* 108:198102-1-5.
31. Huang R, Im SH (2006) Dynamics of wrinkle growth and coarsening in stressed thin films. *Phys Rev E Stat Nonlin Soft Matter Phys* 74:026214.
32. Cerda E, Mahadevan L (2003) Geometry and physics of wrinkling. *Phys Rev Lett* 90: 074302.
33. Hamon MA, Stanley NR, Britton RA, Grossman AD, Lazazzera BA (2004) Identification of AbrB-regulated genes involved in biofilm formation by Bacillus subtilis. *Mol Microbiol* 52:847–860.
34. Camp AH, Losick R (2009) A feeding tube model for activation of a cell-specific transcription factor during sporulation in Bacillus subtilis. *Genes Dev* 23:1014–1024.
35. López D, Vlamakis H, Losick R, Kolter R (2009) Cannibalism enhances biofilm development in Bacillus subtilis. *Mol Microbiol* 74:609–618.
36. Toyama Y, Peralta XG, Wells AR, Kiehart DP, Edwards GS (2008) Apoptotic force and tissue dynamics during Drosophila embryogenesis. *Science* 321:1683–1686.
37. Jarmer H, Berka R, Knudsen S, Saxild HH (2002) Transcriptome analysis documents induced competence of Bacillus subtilis during nitrogen limiting conditions. *FEMS Microbiol Lett* 206(2):197–200.
38. Abràmoff MD, Hospitals I, Magalhães PJ, Abràmoff M (2004) Image processing with ImageJ. *Biophotonics International* 11(7):36–42.
39. Orteu J-J (2009) 3-D computer vision in experimental mechanics. *Opt Lasers Eng* 47: 282–291.
40. Last JA, Russell P, Nealey PF, Murphy CJ (2010) The applications of atomic force microscopy to vision science. *Invest Ophthalmol Vis Sci* 51:6083–6094.